Stem Cell Reports
Article

ISSCR

OPEN ACCESS

Deciphering heterogeneous populations of migrating cells based on the computational assessment of their dynamic properties

Aymeric Ferreira,[1,2,5] Cedric Bressan,[1,3,5] Simon V. Hardy,[1,2,4,*] and Armen Saghatelyan[1,3,*]
[1]CERVO Brain Research Center, Quebec City, QC G1J 2G3, Canada
[2]Department of Biochemistry, Microbiology, and Bioinformatics, Université Laval, Quebec City, QC G1V 0A6, Canada
[3]Department of Psychiatry and Neuroscience, Université Laval, Quebec City, QC G1V 0A6, Canada
[4]Department of Computer Science and Software Engineering, Université Laval, Quebec City, QC G1V 0A6, Canada
[5]These authors contributed equally
*Correspondence: simon.hardy@ift.ulaval.ca (S.V.H.), armen.saghatelyan@fmed.ulaval.ca (A.S.)
https://doi.org/10.1016/j.stemcr.2022.02.011

SUMMARY

Neuronal migration is a highly dynamic process, and multiple cell movement metrics can be extracted from time-lapse imaging datasets. However, these parameters alone are often insufficient to evaluate the heterogeneity of neuroblast populations. We developed an analytical pipeline based on reducing the dimensions of the dataset by principal component analysis (PCA) and determining sub-populations using k-means, supported by the elbow criterion method and validated by a decision tree algorithm. We showed that neuroblasts derived from the same adult neural stem cell (NSC) lineage as well as across different lineages are heterogeneous and can be sub-divided into different clusters based on their dynamic properties. Interestingly, we also observed overlapping clusters for neuroblasts derived from different NSC lineages. We further showed that genetic perturbations or environmental stimuli affect the migratory properties of neuroblasts in a sub-cluster-specific manner. Our data thus provide a framework for assessing the heterogeneity of migrating neuroblasts.

INTRODUCTION

Cell migration is an essential process underlying normal brain development, and its alterations lead to severe neurodevelopmental disorders (Klingler et al., 2021). Migrating neuronal precursors, also called neuroblasts, are bipolar cells with a long leading process extending from the cell body in the direction of migration as well as a short trailing process (Kaneko et al., 2017). During cell migration, the shape of the neuroblast constantly changes as migration progress through a cycle of extension and retraction of the leading process interspersed by nucleus translocation (nucleokinesis) and cell body movement (Kaneko et al., 2017). Cell migration is a discontinuous process composed of migratory phases interrupted by stationary phases (Bressan et al., 2020; Snapyan et al., 2009).

While neuronal migration largely ceases after embryonic and early postnatal development, it is preserved in certain regions of the adult brain associated with postnatal neurogenesis (Bressan and Saghatelyan, 2021). During rodent adult olfactory neurogenesis, thousands of immature neurons transit every day from the subventricular zone (SVZ) to the olfactory bulb (OB) along the rostral migratory stream (RMS). These migrating neuroblasts originate from neural stem cells (NSCs) in the SVZ (Doetsch et al., 1999). NSCs divide and give rise to transient-amplifying progenitors (TAPs), which in turn rapidly divide to generate neuroblasts (Alvarez-Buylla and García-Verdugo, 2002). In the OB, neuroblasts differentiate and mature into different types of interneurons in the granule and periglomerular cell layers (Malvaut and Saghatelyan, 2016). Interestingly, these different types of bulbar interneurons are derived from heterogeneous populations of NSCs in the SVZ that can be distinguished on the basis of their molecular signatures, sub-region localization, and responses to distinct micro-environmental cues (Cebrian-Silla et al., 2021; Hack et al., 2005; Kelsch et al., 2007; Merkle et al., 2007, 2014). For example, sub-region-specific viral labeling methods have been used to show that NSCs in the dorsal and ventral SVZ generate interneurons in the superficial and deep granule cell layers of the OB, respectively (Alvarez-Buylla et al., 2008; Delgado and Lim, 2015; Merkle et al., 2007), whereas tyrosine hydroxylase (TH)-expressing periglomerular neurons are derived from NSCs in the RMS (Hack et al., 2005; Merkle et al., 2007). At the population level, it has also been shown that OB interneurons derived from Glast$^+$ or Nestin$^+$ NSC lineages display differences in integration and long-term maintenance in the OB (Lagace et al., 2007; Ninkovic et al., 2007). Although all these studies have shown that NSCs are molecularly heterogeneous, less is known about differences in the molecular make-up of neuroblasts migrating from the SVZ to the OB. Only recently has it been shown that neuroblasts in the dorsal and ventral SVZ are heterogeneous and that they can be characterized by distinct molecular signatures (Cebrian-Silla et al., 2021). The molecular diversity of neuroblasts traveling along the RMS remains to be determined. It is conceivable, however, that distinct sub-types of neuroblasts defined by specific molecular profiles are also present in the RMS, given that these migrating cells are derived from heterogeneous NSC populations and that previous studies that have shown distinct expression profiles of some molecular cues, such as Pax6, in neuroblasts (Hack et al., 2005; Kohwi et al., 2005).

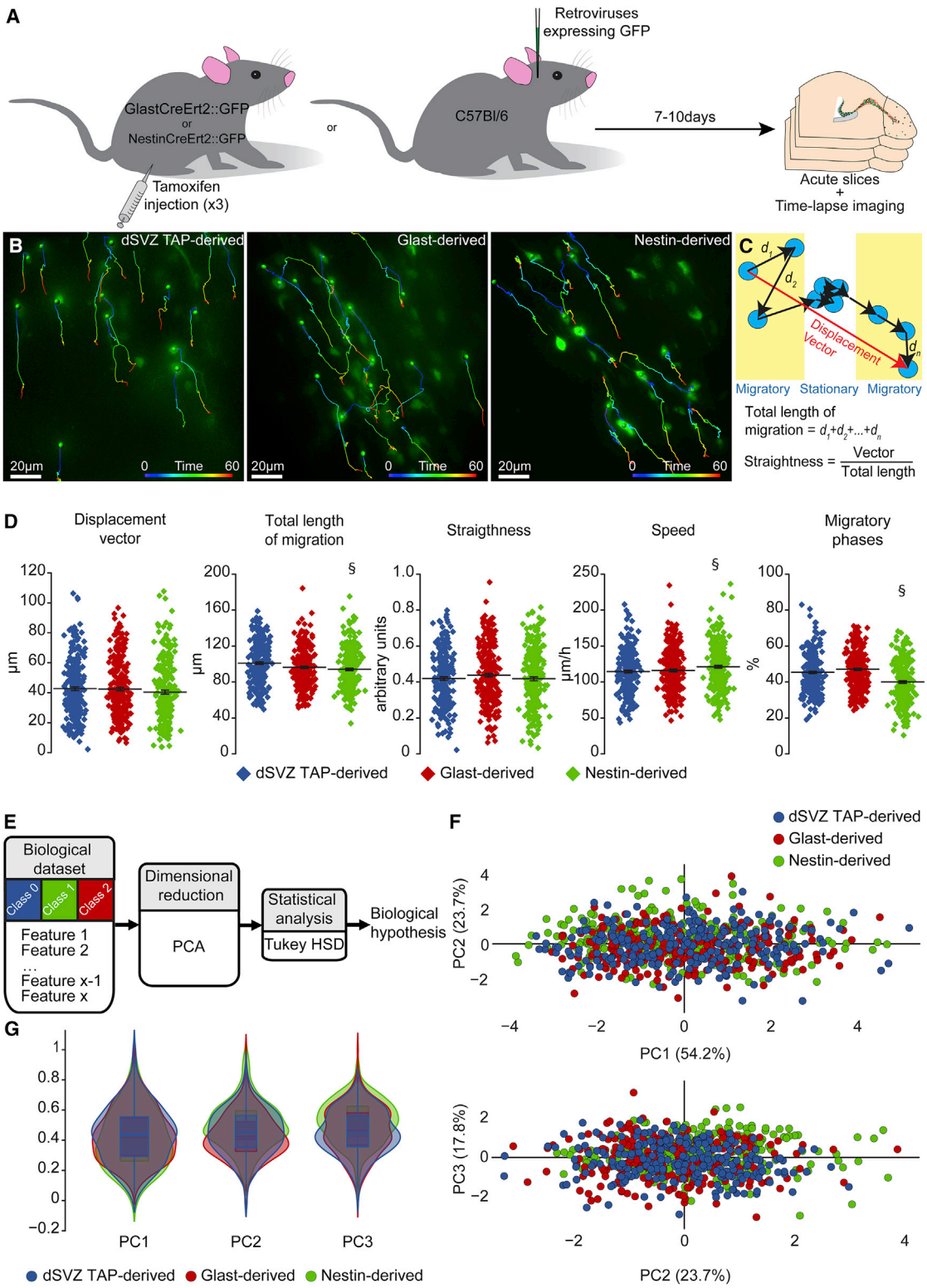

Figure 1. Experimental approach and statistical methods used to evaluate the dynamic properties of neuroblast migration

(A) Experimental design used to label neuroblasts derived from Glast$^+$ and Nestin$^+$ NSC lineages as well as neuroblasts from retrovirally infected dSVZ-TAPs.

(legend continued on next page)

Regardless of the possible molecular heterogeneity of neuroblasts in the RMS, it remains unknown whether neuroblasts have distinct migratory dynamics that may make it possible to categorize them as a functionally heterogeneous population of cells based on their migratory properties.

In the present work, our aim was to determine whether distinct clusters of neuroblasts could be distinguished in the RMS based on their migratory properties. We monitored the migration of neuroblasts derived from Glast$^+$ and Nestin$^+$ lineages and measured migratory parameters such as the displacement vector of migration, total length of the migratory path, straightness, speed of migration, and percentage of the migratory phases. We compared these parameters with those measured in a general population of neuroblasts retrovirally labeled by stereotaxic injection of GFP-encoding retroviruses in the SVZ. On the basis of a standard statistical analysis, we found no major differences between the three different groups. However, after reducing the dimensions of the dataset using a principal component analysis (PCA) and investigating the existence of sub-populations using k-means, a non-parametric clustering technique supported by the elbow criterion method and a decision tree algorithm, to find the appropriate number of clusters, we were able to separate not only three different populations into clusters with distinctive migratory behaviors but also to find common clusters shared by each group. These sub-populations of clusters were affected differently by genetic perturbations or environmental stimuli affecting neuroblast migration. Our data show that migratory neuroblasts are a heterogeneous population of cells displaying specific migratory dynamic signatures within and across the NSC lineages from which they are derived.

RESULTS

Time-lapse imaging of neuroblasts derived from distinct NSC lineages

We studied three different populations of neuroblasts based on their spatial origin or specific lineage. We compared the migration of neuroblasts derived from TAP-labeled cells in the dorsal SVZ (dSVZ-TAPs) as well as from Glast$^+$ and Nestin$^+$ NSC lineages (Lagace et al., 2007; Ninkovic et al., 2007). We labeled the dSVZ-TAPs using GFP-encoding retrovirus injections to infect preferentially rapidly dividing TAPs and their progeny. To label Glast$^+$ and Nestin$^+$ NSCs (hereinafter Glast-derived and Nestin-derived, respectively), we used the transgenic mouse strains Glast-CreERT2::GFP and Nestin-CreERT2::GFP in which GFP is expressed in Glast$^+$ or Nestin$^+$ cells and their progeny following tamoxifen injection (Figure 1A). Time-lapse imaging of acute brain slices for 1 h allowed us to follow the dynamics of cell migration (Figure 1B and Video S1). We measured five parameters: the displacement vector of migration, which is the vector between the first and the last positions of the cell; the total length of the migratory phases; the straightness of migration, calculated as the vector displacement divided by the total length; the percentage of the migratory phases; and the mean speed of migration during the migratory phases (Figure 1C). We analyzed a total of 252 cells (from nine mice) from the dSVZ-TAP population, 267 cells (from 13 mice) from Glast-derived populations, and 249 cells (from 10 mice) from Nestin-derived populations, for a total of 768 cells (Figure 1D). No statistical differences were found between the dSVZ-TAP and Glast-derived populations for any of the parameters studied (Figure 1D). Some differences were observed between the Nestin-derived population and the two other populations, especially for total length, speed, and percentage of the migratory phases. However, the size effect indicator for the speed and total length reported a small size effect ($\eta 2 = 0.009$ for speed and $\eta 2 = 0.016$ for total length), indicating that the statistical differences for speed and total length may only be due to the large size of the samples. For the percentage of migratory phases, the size effect was moderate ($\eta 2 = 0.07$), indicating that, if there was a statistical difference between the Nestin-derived population and the two other populations, the difference was not stringent and could be at least partially attributed to the sampling size. These results suggest that it is difficult to

(B) Example of time-lapse imaging of GFP$^+$ neuroblasts of three different groups in acute brain sections and analysis of their dynamic properties.

(C) Schema showing the distinct migratory parameters used to analyze the dynamics of cell migration.

(D) Total length of migration, displacement vector, speed of migration, straightness, and percentage of the migratory phases of dSVZ-TAP-derived, Glast-derived, and Nestin-derived neuroblasts (n = 252 cells for the dSVZ-TAP population, 267 for the Glast-derived population, and 249 for the Nestin-derived population). $^{\S}p < 0.01$ with a one-way ANOVA followed by a Tukey-HSD post hoc test.

(E) General pipeline to analyze biological data and highlight differences based on a combination of dimension reduction and statistical methods.

(F) PCA of dSVZ-TAP-derived (blue), Glast-derived (red), and Nestin-derived (green) populations.

(G) Representation of the three biggest principal components obtained by reducing the five features to three principal components with the highest variance.

See also Video S1

separate different populations of neuroblasts on the basis of different parameters of migration using a standard statistical analysis.

A correlation analysis of the migratory parameters revealed a strong correlation (0.7–0.89 [Schober et al., 2018]) between straightness and the displacement vector of migration and a moderate correlation (0.4–0.69 [Schober et al., 2018]) between total length, displacement vector, and speed (Figure S1A). The percentage of the migratory phases seemed uncorrelated to the other parameters of cell migration. To reduce the potential bias in the analysis and improve the visualization of the results, we used a principal component analysis (PCA) to reduce the correlation between the features and analyze non-correlated components (Figures 1E–1G). After the PCA, we were able to group more than 95% of the variance into only three features. Principal component (PC)1 grouped 54.2% of the variance and was mainly related to total length, speed, and displacement vector (Figure 1F). An increase along the PC1 axis corresponded to an increase in the displacement vector and straightness. PC2 grouped 23.7% of the variance and was predominantly related to the percentage of the migratory phases, speed, and total length of migration (Figure 1F). The percentage of the migratory phases decreased along the PC2 axis, whereas speed and total length increased, meaning that high PC2 values were related to cells with high speed and total length but with relatively low values for the percentage of time in the migratory phases. Last, PC3 grouped 17.8% of the variance. The percentage of the migratory phases and total length were the two main features associated with this axis (Figure 1F). When PC3 increased, total length and the percentage of the migratory phases increased. The cells with a high PC3 value traveled over a long distance and were predominantly in the migratory phase. After dimension reduction, we analyzed the variance by ANOVA followed by Tukey's honestly significant difference (Tukey-HSD) post hoc test to validate the differences between the three populations (Figure 1G). Although we observed no significant differences in PC1 and PC2 among the three populations, there was a significant difference in PC3 ($p < 0.05$) between the Nestin-derived and the dSVZ-TAP-derived populations and between the Nestin-derived and the Glast-derived populations. We observed no difference between the dSVZ-TAP-derived and the Glast-derived populations even after dimension reduction. These results indicate that neuroblast populations of different origins are difficult to separate based on the migratory properties of the total population.

Neuroblasts derived from three different lineages can be sub-divided into distinct and overlapping sub-clusters inside and across different populations

Although our data revealed no statistical differences in the various migratory parameters of neuroblasts derived from the three different lineages, the large variance of values and the nonnormal distribution of the samples within each group raised the possibility of the presence of sub-clusters within each population. To compare neuroblasts from the three different origins and to detect potential sub-clusters, we performed a clustering analysis with the k-means algorithm (Figure 2A). The number of clusters in k-means was determined using the elbow criterion method (Figure S1B). There was an elbow for both Nestin-derived and Glast-derived neuroblasts, indicating that a division into two clusters was more likely (Figure S1B, red and green arrows). For the dSVZ-TAP population, an elbow was observed for three clusters (Figure S1B, blue arrow), although a small elbow was also noticeable for two clusters. To validate the number of clusters for each population, we used a decision tree, which also makes it possible to interpret which PCs are used by the k-means algorithm for clustering criteria (Figure 2B). The decision tree had a maximal depth of four and was trained with the three main PCs of the migratory parameters. The categorization by the decision tree of Glast-derived and Nestin-derived populations into two clusters used all three PCs and covered 95.7% of the data variance (Figure 2B). However, the separation of the dSVZ-TAP population into two clusters was based only on PC1 and accounted for only 54.2% of the data variance. This suggested that the division of the dSVZ-TAP population into two clusters was sub-optimal and that a higher number of sub-clusters was more likely, as also suggested by the elbow criteria (Figure S1B, blue arrow). We thus categorized the dSVZ-TAP population by the decision tree into three clusters (Figure 2B). This categorization revealed that all three PCs are used for sub-divisions that account for 95.7% of the total variance of the data (Figure 2B). These data suggested that the minimal number of clusters that best represent the data are two clusters for the Nestin-derived and Glast-derived populations and three clusters for the dSVZ-TAP population. After establishing the presence of different clusters within each population of neuroblasts, we determined the statistical significance of the similarity for each cluster using a one-way ANOVA followed by a Tukey-HSD post hoc test. P values lower than 0.05 were considered significant (Figure 2C). We found a common cluster in the three different populations of neuroblasts that was overlapping and statistically similar in all three PCs (clusters T3, G1, and N1 in Figures 2C and 2D). The two other clusters of dSVZ-TAPs (T1 and T2) and the other clusters of Glast-derived (G2) and Nestin-derived (N2) neuroblasts were non-overlapping and showed no equivalence across the different lineages (Figures 2C and 2D). Our data highlight the existence of a common overlapping subpopulation of highly motile cells that is shared by the different neuroblast populations (Figure S1C) as

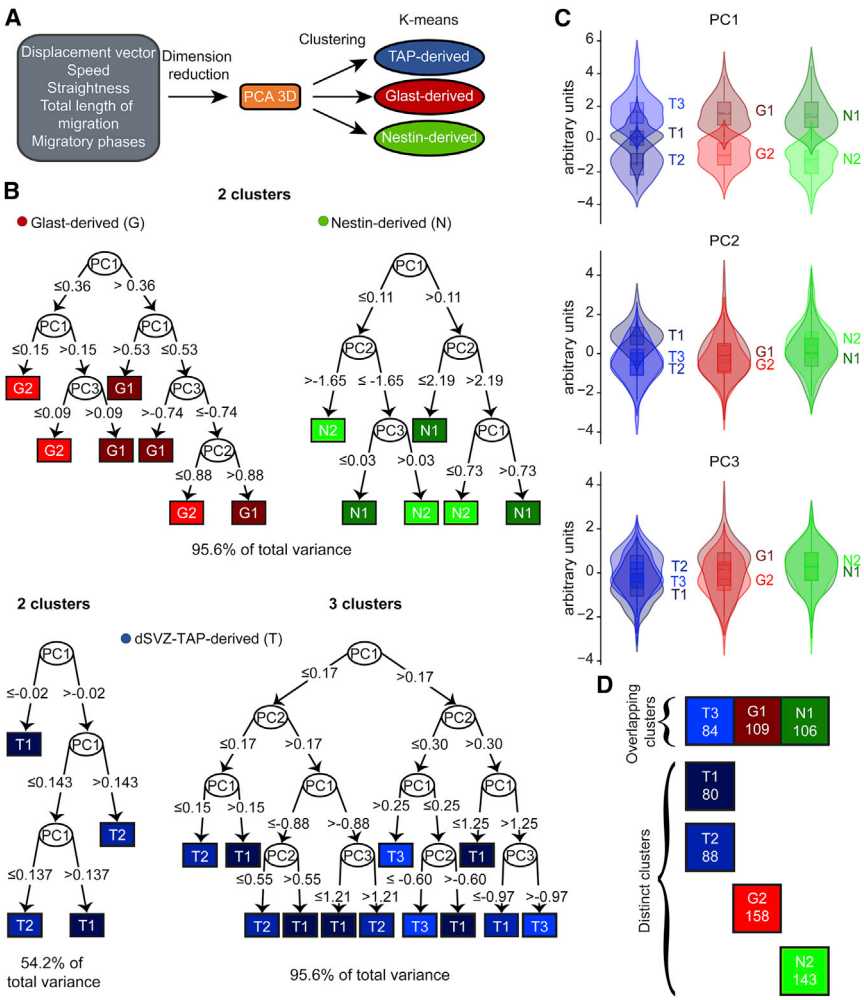

Figure 2. Analysis of clusters for neuroblasts derived from three different lineages

(A) Schema of the analytical pipeline used to investigate the presence of sub-clusters in three neuroblast populations.

(B) Predicted classes and decision tree to separate the data into two or three clusters. Each node represents the PC used to separate the data, and each arrow indicates the threshold value used to divide the samples.

(C) Violin plot representation of each principal component after dimension reduction and normalization for three dSVZ-TAP sub-clusters (blue), two Glast-derived sub-clusters (red), and two Nestin-derived sub-clusters (green).

(D) Statistically distinct and overlapping clusters between each population after reduction by PCA and subdivision into three clusters for dSVZ-TAP, two clusters for Glast-derived, and two clusters for Nestin-derived neuroblasts obtained by ANOVA followed by a Tukey-HSD test. p values < 0.05 were considered significant. The numbers inside each sub-cluster indicate the number of neuroblasts in each cluster.

See also Figures S1 and S2

well as the presence of separate clusters of cells with various behaviors depending on their lineage.

It should be noted, however, that all of the clusters that we have identified so far were distinct only on PC1, which represented 54.2% of the variance. Furthermore, the violin plot representations of the T2, T3, G1, G2, N1, and N2 clusters followed bimodal distributions (Figure 2C) (Hintze and Nelson, 1998). We thus determined whether doubling the number of clusters would reveal more sub-populations with distinctive migratory features comprised in other PCs. Indeed, a subdivision into six clusters for dSVZ-TAP, four for Glast-derived, and four for Nestin-derived neuroblasts divided these populations into clusters with a normal distribution and used all the variance in the dataset (Figure 3A). For example, the N1 and N2 clusters had a high degree of similarity and could only be separated through PC2, which contained 23.7% of the variance. This additional clustering did not affect the presence of previous overlapping clusters. For example, the cluster on the top of PC1 was still present in all three populations of neuroblasts (T2, G4, and N4 in Figure 3), with no statistically significant differences.

On the basis of this new clustering analysis, we wondered whether the sub-clusters we had identified had distinct migration properties. The clusters with high values along PC1 (T2, G4, N4) contained the neuroblasts with the highest values for displacement vector, total length, and straightness (Figure 3B). Their speed and percentage of migratory phases were also particularly high. The bottom clusters in PC1 (T1, T5, N3, and G1) were composed of cells with the lowest values for displacement vector and total length. We also observed a difference between the two groups of clusters, with T1 and N3 having a very low percentage of migratory phases, with a mean of 33.4 and 33.6%, respectively, and T5 and G1 having a higher value of percentage of migratory phases, with a mean of 48.6 and 48.7%, respectively (Figure 3B). Last, G2 and N2 had relatively low values for speed (111 and 108 μm/h, respectively), total length (88.5 and 90.3 μm, respectively), and displacement vector (49.1 and 43.3 μm, respectively) but

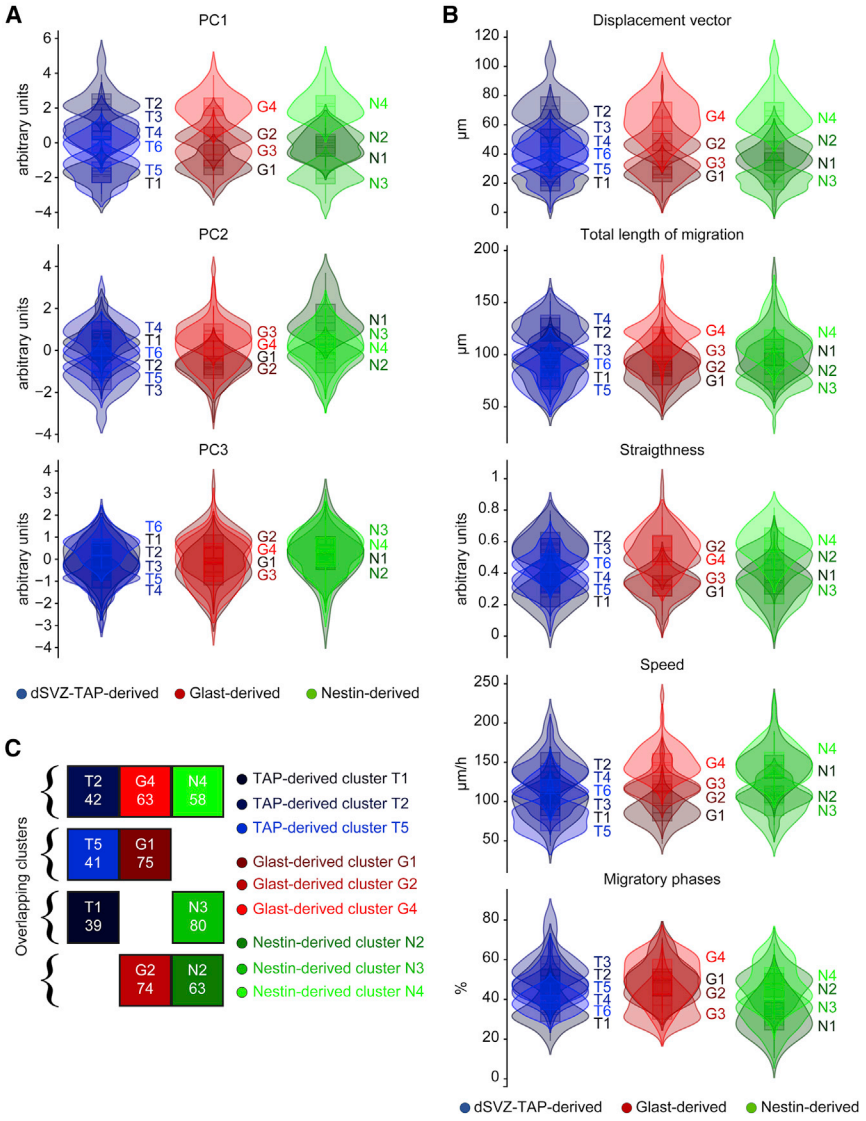

Figure 3. Analysis of three neuroblast populations with a greater number of clusters

(A) Violin plot representation of each PC after dimension reduction and normalization for six dSVZ-TAP sub-clusters (blue), four Glast-derived sub-clusters (red), and four Nestin-derived sub-clusters (green).

(B) Violin plot representation of each feature of cell migration after dimension reduction and normalization for six dSVZ-TAP sub-clusters (blue), four Glast-derived sub-clusters (red), and four Nestin-derived sub-clusters (green).

(C) Statistically similar clusters between each population after reduction by PCA and subdivision into six clusters for dSVZ-TAP, four clusters for Glast-derived, and four clusters for Nestin-derived neuroblasts obtained by ANOVA followed by a Tukey-HSD post hoc analysis; p values < 0.05 were considered significant.

higher mean values for percentage of migratory phases (48.7 and 47.5%, respectively). The clusters without any equivalence across the different lineages were characterized by different properties. For example, G3 and N1 were similar with respect to total length, displacement vector, straightness, and migratory phases (Figure 3B). However, while these two clusters were characterized by quite low values for all these parameters, they had different speeds of migration, (126 µm/h for G3 and 146 µm/h for N1) (Figure 3B). T3 was like N2 and G2 in terms of speed, straightness, and total length but was characterized by a higher percentage of migratory phases (Figure 3B). T4 and T2 were very similar with respect to some parameters but displayed a marked difference in displacement vectors (25.4 µm for T4 and 73.0 µm for T2) and straightness (0.34 for T4 and 0.59 for T2) (Figure 3B). All together, the analytical pipeline we developed revealed the heterogeneous nature of the sub-populations of neuroblasts derived from the same lineage. Furthermore, our data also showed that neuroblasts derived from different lineages may share similar properties of cell migration, implying the presence of common determinants for regulating the dynamics of neuroblasts derived from molecularly distinct NSCs.

Genetic and environmentally induced changes in adult neurogenesis and neuronal migration affect the migratory properties of neuroblasts in specific sub-clusters

After establishing the analytical pipeline, we next determined whether genetic or environmental manipulations that either decrease or increase neuronal migration and adult neurogenesis would alter the migration of all

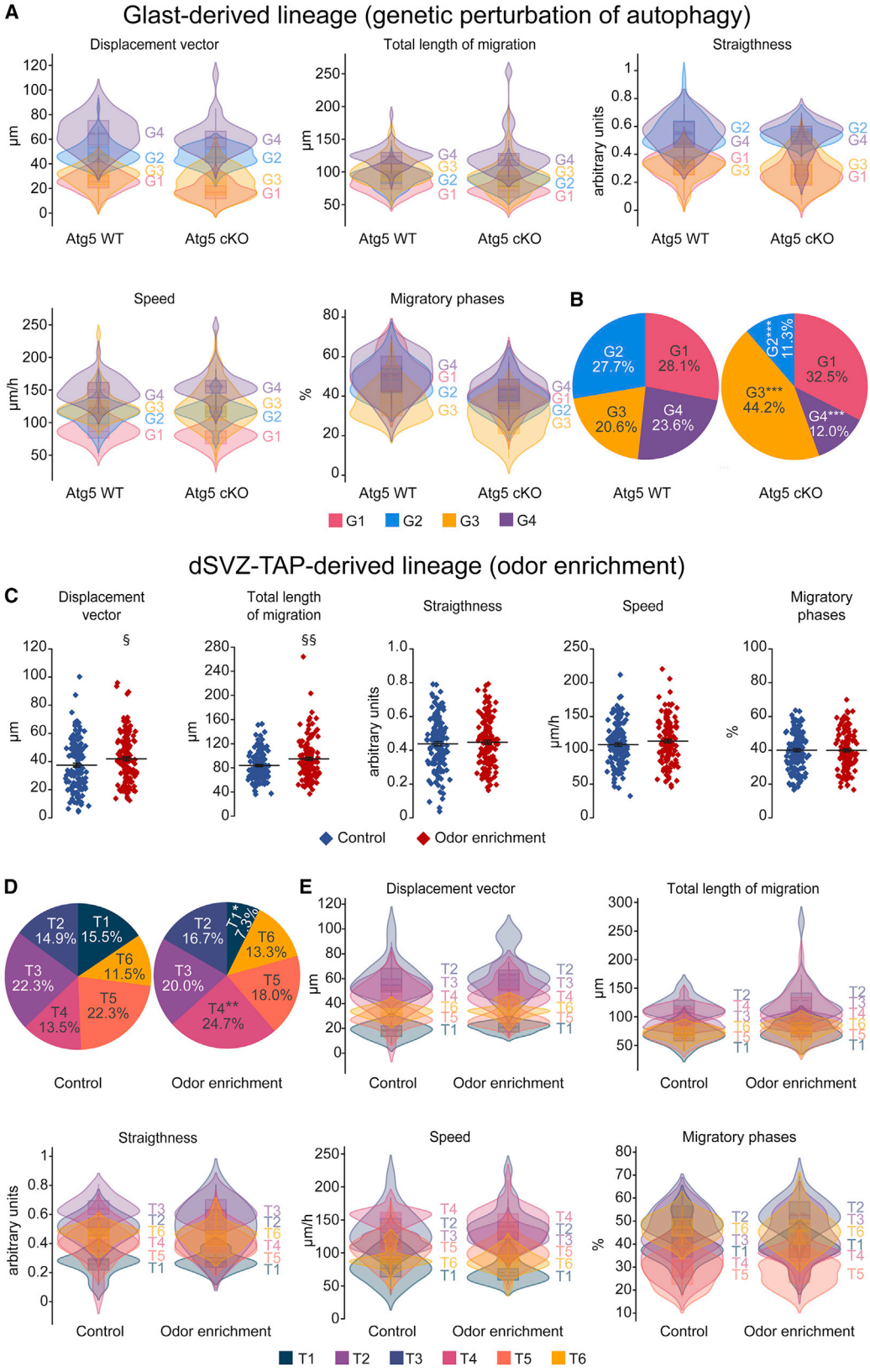

(legend on next page)

neuroblasts or only those belonging to specific sub-clusters. We have previously shown that the genetic perturbation of autophagy, a major cellular homeostasis pathway that controls protein and organelle degradation and recycling (Yang and Klionsky, 2010), affects neuronal migration by altering the pace and periodicity of the stationary and migratory phases (Bressan et al., 2020; Bressan and Saghatelyan, 2020). Although, at the population level, tamoxifen-inducible deletion of Atg5, a key autophagic protein, in Glast-derived lineage (GlastCreErt2::Atg5$^{fl/fl}$::GFP, hereafter, Atg5 cKO) reduces the overall distance of cell migration and the percentage of the migratory phases (Bressan et al., 2020), it remains to be determined how altered autophagy affects the dynamic properties of neuroblasts from distinct sub-clusters. We thus performed clustering with the previously trained k-means estimator for the Glast lineage (Figure 2A) to analyze neuroblasts in Atg5 cKO and Atg5 WT (GlastCreErt2::Atg5$^{w/w}$::GFP) mice. Our data revealed that the Atg5 deletion affects neuroblasts in distinct sub-clusters differently (Figure 4A). The G4 and G2 clusters were particularly affected by the Atg5 deletion. In Atg5 WT mice, these clusters accounted for 51.3% of the neuroblasts of the total population (Figure 4B), whereas in Atg5 cKO mice they accounted for only 23.3% of the total population ($p < 0.001$ with Agresti-Caffo test). In Atg5 WT mice, the G4 and G2 clusters were characterized by the highest displacement vector values (65.6 and 49.2 μm, respectively) because of higher mean values for the percentage of migratory phases (50.5 and 48.7%, respectively). On the other hand, the number of Atg5 cKO neuroblasts in the G3 cluster that were characterized by lower displacement vector, lowest straightness, and percentage of migratory phases values increased from 20.6% in Atg5 WT to 44.2% in Atg5 cKO mice (Figure 4B). No differences were observed in the G1 cluster, which is characterized by cells migrating with low speed (Figure 4B). These data suggest that an autophagy deficiency predominantly affects highly motile neuroblasts with high displacement vector values and frequently occurring migratory phases.

We then determined whether environmental changes that boost adult neurogenesis also affect neuronal migration and, if so, whether these changes occur in a sub-cluster-specific manner. To address this issue, we kept mice that had previously been injected with GFP-encoding retroviruses in an odor-enriched environment. Every day for 7–9 days, the mice were exposed to a single natural odor for 24 h. The control mice were kept under the same conditions without, however, being exposed to the natural odor. Although it has been previously shown that odor enrichment increases adult OB neurogenesis (Rochefort et al., 2002), it is not known how it affects neuronal migration. Time-lapse imaging of dSVZ-TAP-derived neuroblasts in acute brain slices revealed that odor enrichment induces small albeit statistically significant differences in the displacement vector and total length ($p < 0.05$ and $p < 0.001$, respectively, with an unpaired t test; Figure 4C). To determine whether these differences resulted from the sampling size (n = 148 and 150 cells for the control and odor-enriched groups, respectively), we calculated Cohen'|'s coefficient. The Cohen'|'s coefficients for displacement vector and total length were small to moderate (0.26 and 0.4, respectively), indicating that these differences were not stringent and could be attributed to the sampling size. We thus performed a clustering analysis. Since the dSVZ-TAP population in these experiments was imaged 7–9 days later compared with those shown in Figure 2A, we obtained a new k-means estimator. Our analysis showed that odor enrichment affects neuroblasts of distinct sub-clusters differently (Figure 4D). Whereas T1 and T4 clusters were significantly affected, T2, T3, T5, and T6 clusters were unchanged (Figure 4D). In the control mice, the T1 and T4 clusters accounted for 15.5% and 13.5%, respectively, of the total population of migrating cells, whereas in mice exposed to odor-enriched environment, these clusters accounted for 7.3% and 24.7% of the total population of neuroblasts ($p < 0.05$ and $p < 0.01$ with Agresti-Caffo test; Figure 4D). Interestingly, T4 and T1 clusters were characterized by the highest and lowest values of the speed of migration (149.6 and 73.3 μm/h,

Figure 4. Genetic and environmental factors affect neuronal migration in a sub-cluster-specific manner

(A) Violin plot representation of each feature of cell migration after dimension reduction and normalization for four Glast-derived neuroblast sub-clusters in Atg5 cKO and Atg5 WT mice.

(B) Pie chart representation of the percentage of each sub-cluster in Atg5 cKO and Atg5 WT mice. Note the decrease in the number of neuroblasts in the G2 and G4 clusters and the concomitant increase in the G3 cluster following conditional Atg5 deletion.

(C) Total length of migration, displacement vector, speed of migration, straightness, and percentage of the migratory phases of neuroblasts in the control group and following odor enrichment (n = 148 cells and 150 for the control and odor-enriched groups, respectively). $^{§}p < 0.05$ and $^{§§}p < 0.001$ with an unpaired t test.

(D) Pie chart representation of the percentage of neuroblasts in each sub-cluster showing increased number of migrating cells in the T4 cluster and decreased number of cells in the T1 cluster following odor enrichment.

(E) Violin plot representation of each feature of cell migration after dimension reduction and normalization for six dSVZ-TAP-derived sub-clusters for control and odor-enriched mice.

respectively; Figure 4E), whereas their migratory phases were quite similar (32.0% and 39.8%, respectively). Following odor enrichment, the number of neuroblasts was increased in the T4 cluster and decreased in the T1 cluster, indicating that odor enrichment increased the motility of neuroblasts having low speed of migration (Figure 4D). These data reveal sub-cluster-specific changes in the neuroblasts' migration following odor enrichment.

DISCUSSION

We show that neuroblasts in the RMS, which are generally considered to be a homogeneous population of cells, can be sub-divided into distinct clusters based on their migratory characteristics by using PCA and k-means. Although previous studies have attempted to assess the diversity of neuroblast populations based on their morphological properties (i.e., branching of the leading and trailing processes) or their speed of migration (Belvindrah et al., 2017), those reports used only a single parameter for cell morphology/migration and did not encompass the entire panoply of dynamic features of migrating cells. Furthermore, the migratory morphology of cells is not predictive of their motility (Nam et al., 2007). To address this issue, we developed an analytical pipeline to reveal the heterogeneous nature of neuroblasts. We identified distinct clusters of neuroblasts derived from distinct NSC lineages as well as clusters inside each lineage. On the other hand, a statistically similar, overlapping cluster of neuroblasts was also present in all three lineages.

We applied our pipeline of dimensional reduction to a whole set of migratory parameters and observed that whereas PC1 was mostly determined by a combination of total length, speed, and displacement vector, PC2 was governed by speed, total length, and percentage of migratory phases, while PC3 was mostly guided by the percentage of migratory phases and total length. The elbow criterion method validated by a decision tree algorithm indicated that the dSVZ-TAP population can be sub-divided into three clusters, whereas Glast-derived and Nestin-derived neuroblasts can be sub-divided into two clusters. This subdivision was mostly determined by the PC1 component, while doubling the number of clusters for each population led to the emergence of clusters of cells defined by the PC2 and PC3 components (Figure 3). Interestingly, the common clusters for neuroblasts derived from the three different lineages could be attributed to very motile cells with high speed, high displacement vector, and high straightness values. At the opposite end of the spectrum, we found two clusters containing cells with lower motility in the dSVZ-TAP-derived neuroblast population (T5 and T1) that have homologs in the Glast-derived (G1) and Nestin-derived (N3) populations. Interestingly, only 50% of the clusters of dSVZ-TAP-derived cells were equivalent to either Glast-derived or Nestin-derived populations or to both. These results suggest that neuroblasts derived from several other lineages are present in the RMS and may encompass the remaining 50% of dSVZ-TAP-derived cells. Indeed, NSCs in the SVZ are heterogeneous and are defined by specific molecular signatures and spatiotemporal localizations in the neurogenic niche (Codega et al., 2014; Hack et al., 2005; Merkle et al., 2007). Since we analyzed only two lineages, the dynamic properties of neuroblasts derived from other NSC lineages need to be investigated. It should also be noted that while NSC lineages are characterized by distinct molecular signatures, they are also overlapping (Bottes et al., 2021; Codega et al., 2014). The common cluster in Glast-derived and Nestin-derived neuroblasts suggests that common molecular determinants that regulate the dynamic properties of migrating cells are present in these neuroblasts. It remains to be determined how distinct neuroblast clusters that are defined by their dynamic properties correspond to neuroblast clusters that are defined by their molecular signatures.

On the other hand, even while the dSVZ-TAP population encompassed a broader range of cells based on their migration properties, some Glast-derived (G2, G3) and Nestin-derived (N1, N2) clusters did not overlap with any dSVZ-TAP clusters. The neuroblasts in the dSVZ-TAP population were derived by virally labeling TAPs in the dSVZ. This indicated that neuroblasts originating from NSCs in other spatial locations of the neurogenic niche are not labeled by this approach. It is thus conceivable that neuroblast heterogeneity is far more diverse than described herein and that further studies will be required to determine the full complexity of these migrating cells. This can be achieved either by virally labeling distinct sub-domains of the neurogenic niche or by using a more general reporter of migrating neuroblasts such as doublecortin (DCX). For example, upon Cre recombination, migrating neuroblasts can be labeled in DCX-CreERT2 mice independently of their origin (Zhang et al., 2010).

Are distinct neuroblast sub-clusters differently affected by genetic factors or environmental stimuli? Our genetic and environmental manipulations, which are known to modulate adult OB neurogenesis and neuronal migration (Bressan et al., 2020; Rochefort et al., 2002), revealed that there are distinct effects on different neuroblast sub-clusters that point to the presence of a functionally distinct set of neuroblasts that migrate with distinct dynamics and that are sensitive to different stimuli. Inducible genetic deletion of Atg5, a key protein involved in autophagy, decreased neuroblast migration in the G2 and G4 clusters, which are characterized by a high percentage of migratory phases. We have previously shown that in migrating

neuroblasts autophagy is induced by AMP kinase (Bressan et al., 2020), a major energy sensor in cells that detects changes in cellular ATP/ADP levels (Herzig and Shaw, 2018). Time-lapse imaging of ATP/ADP levels in migrating neuroblasts has shown that decreases in ATP levels during cell migration result in the entry of cells into the stationary phase and the induction of autophagy to sustain cellular homeostasis and neuronal migration (Bressan et al., 2020; Bressan and Saghatelyan, 2020). The highly motile nature of neuroblasts in the G2 and G4 clusters, which display frequently occurring migratory phases, would likely lead to higher energy metabolism, making them particularly sensitive to autophagy-dependent regulation of neuronal migration. This is consistent with the data presented herein showing that the G2 and G4 clusters are especially vulnerable to autophagy deficiency. On the other hand, odor enrichment increased the number of neuroblasts in the T4 cluster, which is characterized by a high total length and speed of migration, at the expense of less motile neuroblasts in the T1 cluster. It should be noted that, although it has been previously shown that odor enrichment increases the survival of adult-born neurons in the OB (Rochefort et al., 2002), the effect of odor-enriched environment on neuronal migration was unknown. Our analysis of the total populations of neuroblasts in the control and odor-enriched conditions was confounded by the sampling size and did not reveal stringent statistically significant differences. Only after PCA and clustering analysis we were able to observe changes in specific sub-clusters, underscoring the need to take the heterogeneous nature of migrating neuroblasts into account when assessing the effects of genetic perturbations and/or environmental stimuli on cell migration. All together, our results show that there is a high degree of diversity in migrating neuroblasts. This enabled us to identify several clusters based on their dynamic properties that are regulated differently by genetic factors and environmental stimuli.

EXPERIMENTAL PROCEDURES

Animals

Experiments were performed using 2- to 4-month-old C57BL/6 (Charles River), Glast-CreERT2- GFP, and Nestin-CreERT2-GFP mice. We crossed Glast-CreERT2 (Mori et al., 2006) or Nestin-CreErt2 (Lagace et al., 2007) mice maintained on C57Bl/6 genetic backgrounds with CAG-CAT-GFP reporter mice (Waclaw et al., 2010) maintained on a CD1 genetic background to obtain the experimental animals. For the genetic downregulation of autophagy, we crossed the Glast-CreErt2::GFP line with $Atg5^{fl/fl}$ mice (B_6.129S-*Atg5*<tm1Myok>, RBRC02975, Riken**)** maintained on C57Bl/6 genetic background to obtain the Atg5 WT (Glast-CreErt2::$Atg5^{w/w}$::CAG-CAT-GFP) and Atg5 cKO (Glast-CreErt2::$Atg5^{fl/fl}$::CAG-CAT-GFP) mice. All the experiments were performed with the approval of the Université Laval Animal Protection Committee. The mice were housed in cages under standard conditions, with one to four mice per cage. They were kept on a 12:12-h light/dark cycle at a constant temperature (22°C), with food and water *ad libitum*.

Stereotactic injections

For the stereotactic injections, C57BL/6 mice were anesthetized with isoflurane (2–2.5% isoflurane, 1 L/min of oxygen) and were kept on a heating pad during the entire surgical procedure. The mice were stereotactically injected with a GFP-encoding retrovirus (2.9 × 107 TU/mL, Molecular Tools Platform at the CERVO Brain Research Center) in the dorsal subventricular zone (dSVZ) at the following coordinates (with respect to the bregma): anterior-posterior (AP) 0.70 mm, medio-lateral (ML) 1.20 mm, dorsoventral (DV) 1.90 mm.

Tamoxifen injection

To induce Cre recombination in $Glast^+$ and $Nestin^+$ NSCs and their progeny, Glast-CreERT2-GFP and Nestin-CreERT2-GFP mice were intraperitonially injected with tamoxifen (180 mg/kg, Sigma-Aldrich) once a day for 3 days. The tamoxifen was diluted in sunflower seed oil (Sigma-Aldrich) and anhydrous ethanol (10% final). The mice were used 7–15 days after the last tamoxifen injection.

Odor enrichment

Seven days after the GFP-encoding retrovirus was injected into the dSVZ of C57BL/6 mice, the animals were housed individually and were randomly assigned to the control or odor-enriched group. Mice in the odor enrichment group were exposed daily to natural odors (paprika, turmeric, ginger, vanilla, coffee, cumin, cinnamon, curry, thyme) 24 h a day for 7–9 days. Odors were presented in Petri dishes with a perforated cover placed in the home cages of the mice. Control mice were maintained under the same conditions but were exposed to Petri dishes without odors. The mice were used 7–9 days after the start of the odor enrichment.

Time-lapse imaging

For the time-lapse imaging, acute brain slices were prepared as described previously (Bakhshetyan and Saghatelyan, 2015). Briefly, after anesthesia with ketamine (100 mg/kg) and xylazine (10 mg/kg), the mice were perfused transcardially with modified oxygenated artificial cerebrospinal fluid (ACSF) composed of 210.3 mM sucrose, 3 mM KCl, 2 mM $CaCl_2.2H_2O$, 1.3 mM $MgCl_2.6H_2O$, 26 mM $NaHCO_3$, 1.25 mM $NaH_2PO_4.H_2O$, and 20 mM glucose. The brains were then quickly removed, and 250-μm-thick sections were cut with a vibratome (HM 650V, Thermo Scientific). The sections were kept at 37°C in ACSF composed of 125 mM NaCl, 3 mM KCl, 2 mM $CaCl_2.2H2O$, 1.3 mM $MgCl_2.6H_2O$, 26 mM $NaHCO_3$, 1.25 mM $NaH_2PO_4.H_2O$, and 20 mM glucose under oxygenation for 6–8 h. Imaging was performed using a BX61WI (Olympus) upright microscope. Images were acquired using a 40× water immersion objective (NA = 0.8) every 15–30 s for 1 h with multiple z-stacks (11 stacks at 3-μm intervals). For the imaging, the cells were tracked automatically using Imaris 7.2 software (Bitplane, Oxford Instrument). Vector displacement (vector between the first and last position), total length (sum of the vector

displacement between each time point), and straightness (vector displacement divided by total length) were obtained directly from Imaris. For the calculations of the duration of the migratory phases, the instantaneous speed (speed between two consecutive times points) profile of each individual cell was plotted using Origin software (OriginLab Corporation). To account for both rapidly and slowly migrating cells, the migratory phases were determined manually based on the instantaneous speed profile (Bressan et al., 2020). The percentage of migration was calculated as the sum of the duration of all migratory events during 1 h of imaging. The speed of migration was determined only during the migratory phases.

To ascertain that the migratory dynamic of neuroblasts is unaffected by the time after brain extraction and acute-slice preparation, we compared the dynamic properties of neuroblasts for each of three populations (dSVZ-TAP-derived, Glast-derived, and Nestin-derived) in the slices prepared from the same animal and imaged for 1–2 or 5–6 h after brain extraction. We observed no differences in the dynamics (Figure S2), indicating that migratory parameters of neuroblasts are unaffected by the time of incubation in the ACSF following the brain extraction.

Statistical analysis

The statistical analyses were performed using an ANOVA followed by a Tukey-HSD test or unpaired t test when comparing two groups, with a significance level set at $p < 0.05$. The size effect ($\eta 2$ or Cohen's coefficient, for the ANOVA and t test, respectively) was calculated using IBM SPSS software. PCA (Jackson, 2005; Jolliffe, 1986) was performed using the Python package scikit-learn 0.23.2. Because the migration dataset was not susceptible to the curse of dimensionality (Verleysen and François, 2005), PCA was used to reduce the number of features from five to three independent components. All together, these three PC components contained 95.4% of the variance in the dataset. The differences in clusters (Figure 1B) were validated using ANOVA and Tukey-HSD. The elbow criterion (Yuan and Yang, 2019) was measured for each neuroblast population with the Python package yellowbrick 1.2. The elbow criterion method is an heuristic method used to suggest the most appropriate number of clusters in a dataset and is included in scikit-learn 0.23.2. We computed a score with different seed values to avoid analyzing an outlier score. We applied the k-means clustering method (also available in scikit-learn 0.23.2) to each population to find clusters in the dataset reduced with PCA. K-means produced slightly different results with each execution. To avoid analysis of an outlier, the elbow criterion score was calculated for thousands of k-means runs, and the means and standard deviations of the elbow scores were extracted. The seed of the most representative run was chosen using the following equation:

$$score_i = \sum_{i,k} \frac{(SSE_{ik} - \overline{SSE_k})^2}{k}$$

where SSE is the sum of the squared error, k is the number of clusters, and i is the run. The seed number used for all the analyses, except odor enrichment experiments, was 833,945,720. For the odor enrichment experiment the seed was 1,347,397,374. To perform an analysis that was not variable for each subsequent experiment, we trained k-means for each population (Figure 2B) and used it for all the following analyses (Figures 3 and 4). To confirm and validate the number of clusters, a decision tree was trained using the Python package sklearn-0.23.2, with a maximal depth of four. A decision tree is a tool to identify and visualize the decisions of a clustering algorithm. Each choice is represented as a node, each decision is called a branch, and each extremity is called a leaf. The statistical analyses of the clusters were performed using ANOVA and the Tukey-HSD. An Agresti-Caffo statistical test was used to assess differences in the distribution of neuroblasts between different clusters of Atg5 WT and Atg5 cKO as well as Control and Odor enrichment groups (Agresti and Caffo, 2000).

Data and code availability

The MATLAB code for cluster analysis and visualization of migratory cells is available at SaghatelyanLab/clusterAnalysis

Further information and requests for resources and reagents should be directed to and will be fulfilled by the co-corresponding authors, Simon V. Hardy (simon.hardy@ift.ulaval.ca) and Armen Saghatelyan (armen.saghatelyan@fmed.ulaval.ca).

SUPPLEMENTAL INFORMATION

Supplemental information can be found online at https://doi.org/10.1016/j.stemcr.2022.02.011.

AUTHOR CONTRIBUTIONS

A.F. performed the computational analyses of the datasets of migrating cells. C.B. performed the experiments and the cell-tracking analyses. S.V.H. and A.S. supervised the computational and experimental work, respectively. All the authors discussed the data and co-wrote the manuscript.

CONFLICTS OF INTEREST

The authors declare no competing interests.

ACKNOWLEDGMENTS

We thank Karen Bakhshetyan for imaging of some retrovirally labeled cells, Dr. Camille Besse at the Big Data Research Center (Université Laval) for advice on the clustering analysis, and Dr. Chantal Mérette at the CERVO Brain Research Center (Université Laval) for advice on the statistical analysis. This work was supported by a Canadian Institute of Health Research (CIHR) grant to A.S., National Science and Engineering Research Council of Canada (NSERC) grants to S.V.H. and A.S., and a Le Fonds de recherche du Québec – Nature et technologies (FRQNT) team grant to A.S. and S.V.H.

Received: August 16, 2021
Revised: February 17, 2022
Accepted: February 18, 2022
Published: March 17, 2022

REFERENCES

Agresti, A., and Caffo, B. (2000). Simple and effective confidence intervals for proportions and differences of proportions result from adding two successes and two failures. Am. Stat. *54*, 280–288.

Alvarez-Buylla, A., and García-Verdugo, J.M. (2002). Neurogenesis in adult subventricular zone. J. Neurosci. *22*, 629–634. https://doi.org/10.1523/jneurosci.22-03-00629.2002.

Alvarez-Buylla, A., Kohwi, M., Nguyen, T.M., and Merkle, F.T. (2008). The heterogeneity of adult neural stem cells and the emerging complexity of their niche. Cold Spring Harbor Symp. Quant. Biol. *73*, 357–365. https://doi.org/10.1101/sqb.2008.73.019.

Bakhshetyan, K., and Saghatelyan, A. (2015). Tracking neuronal migration in adult brain slices. Curr. Protoc. Neurosci. *71*, 3.28.1–3.28.13. https://doi.org/10.1002/0471142301.ns0328s71.

Belvindrah, R., Natarajan, K., Shabajee, P., Bruel-Jungerman, E., Bernard, J., Goutierre, M., Moutkine, I., Jaglin, X.H., Savariradjane, M., Irinopoulou, T., et al. (2017). Mutation of the α-tubulin Tuba1a leads to straighter microtubules and perturbs neuronal migration. J. Cell Biol. *216*, 2443–2461. https://doi.org/10.1083/jcb.201607074.

Bottes, S., Jaeger, B.N., Pilz, G.A., Jörg, D.J., Cole, J.D., Kruse, M., Harris, L., Korobeynyk, V.I., Mallona, I., Helmchen, F., et al. (2021). Long-term self-renewing stem cells in the adult mouse hippocampus identified by intravital imaging. Nat. Neurosci. *24*, 225–233. https://doi.org/10.1038/s41593-020-00759-4.

Bressan, C., and Saghatelyan, A. (2020). AMPK-induced autophagy as a key regulator of cell migration. Autophagy *17*, 828–829. https://doi.org/10.1080/15548627.2020.1848120.

Bressan, C., and Saghatelyan, A. (2021). Intrinsic mechanisms regulating neuronal migration in the postnatal brain. Front. Cell. Neurosci. *14*, 620379. https://doi.org/10.3389/fncel.2020.620379.

Bressan, C., Pecora, A., Gagnon, D., Snapyan, M., Labrecque, S., De Koninck, P., Parent, M., and Saghatelyan, A. (2020). The dynamic interplay between ATP/ADP levels and autophagy sustain neuronal migration in vivo. eLife *9*, e56006. https://doi.org/10.7554/eLife.56006.

Cebrian-Silla, A., Nascimento, M.A., Redmond, S.A., Mansky, B., Wu, D., Obernier, K., Romero Rodriguez, R., Gonzalez-Granero, S., García-Verdugo, J.M., Lim, D.A., and Álvarez-Buylla, A. (2021). Single-cell analysis of the ventricular-subventricular zone reveals signatures of dorsal and ventral adult neurogenesis. eLife *10*, e67436. https://doi.org/10.7554/eLife.67436.

Codega, P., Silva-Vargas, V., Paul, A., Maldonado-Soto, A.R., Deleo, A.M., Pastrana, E., and Doetsch, F. (2014). Prospective identification and purification of quiescent adult neural stem cells from their in vivo niche. Neuron *82*, 545–559. https://doi.org/10.1016/j.neuron.2014.02.039.

Delgado, R.N., and Lim, D.A. (2015). Embryonic Nkx2.1-expressing neural precursor cells contribute to the regional heterogeneity of adult V–SVZ neural stem cells. Dev. Biol. *407*, 265–274. https://doi.org/10.1016/j.ydbio.2015.09.008.

Doetsch, F., Caillé, I., Lim, D.A., García-Verdugo, J.M., and Alvarez-Buylla, A. (1999). Subventricular zone astrocytes are neural stem cells in the adult mammalian brain. Cell *97*, 703–716. https://doi.org/10.1016/S0092-8674(00)80783-7.

Hack, M.A., Saghatelyan, A., de Chevigny, A., Pfeifer, A., Ashery-Padan, R., Lledo, P.M., and Gotz, M. (2005). Neuronal fate determinants of adult olfactory bulb neurogenesis. Nat. Neurosci. *8*, 865–872. https://doi.org/10.1038/nn1479.

Herzig, S., and Shaw, R.J. (2018). AMPK: guardian of metabolism and mitochondrial homeostasis. Nat. Rev. Mol. Cell Biol. *19*, 121–135. https://doi.org/10.1038/nrm.2017.95.

Hintze, J.L., and Nelson, R.D. (1998). Violin plots: a box plot-density trace synergism. Am. Stat. *52*, 181–184. https://doi.org/10.1080/00031305.1998.10480559.

Jackson, J.E. (2005). A User's Guide to Principal Components (John Wiley & Sons).

Jolliffe, I.T. (1986). Principal components in regression analysis. In Principal Component Analysis, I.T. Jolliffe, ed. (Springer New York), pp. 129–155. https://doi.org/10.1007/978-1-4757-1904-8_8.

Kaneko, N., Sawada, M., and Sawamoto, K. (2017). Mechanisms of neuronal migration in the adult brain. J. Neurochem. *141*, 835–847. https://doi.org/10.1111/jnc.14002.

Kelsch, W., Mosley, C.P., Lin, C.W., and Lois, C. (2007). Distinct mammalian precursors are committed to generate neurons with defined dendritic projection patterns. PLoS Biol. *5*, e300. https://doi.org/10.1371/journal.pbio.0050300.

Klingler, E., Francis, F., Jabaudon, D., and Cappello, S. (2021). Mapping the molecular and cellular complexity of cortical malformations. Science *371*, eaba4517. https://doi.org/10.1126/science.aba4517.

Kohwi, M., Osumi, N., Rubenstein, J.L., and Alvarez-Buylla, A. (2005). Pax6 is required for making specific subpopulations of granule and periglomerular neurons in the olfactory bulb. J. Neurosci. *25*, 6997–7003. https://doi.org/10.1523/JNEUROSCI.1435-05.2005.

Lagace, D.C., Whitman, M.C., Noonan, M.A., Ables, J.L., DeCarolis, N.A., Arguello, A.A., Donovan, M.H., Fischer, S.J., Farnbauch, L.A., Beech, R.D., et al. (2007). Dynamic contribution of nestin-expressing stem cells to adult neurogenesis. J. Neurosci. *27*, 12623–12629. https://doi.org/10.1523/jneurosci.3812-07.2007.

Malvaut, S., and Saghatelyan, A. (2016). The role of adult-born neurons in the constantly changing olfactory bulb network. Neural Plast. *2016*, 1614329. https://doi.org/10.1155/2016/1614329.

Merkle, F.T., Mirzadeh, Z., and Alvarez-Buylla, A. (2007). Mosaic organization of neural stem cells in the adult brain. Science *317*, 381–384. https://doi.org/10.1126/science.1144914.

Merkle, F.T., Fuentealba, L.C., Sanders, T.A., Magno, L., Kessaris, N., and Alvarez-Buylla, A. (2014). Adult neural stem cells in distinct microdomains generate previously unknown interneuron types. Nat. Neurosci. *17*, 207–214. https://doi.org/10.1038/nn.3610.

Mori, T., Tanaka, K., Buffo, A., Wurst, W., Kuhn, R., and Gotz, M. (2006). Inducible gene deletion in astroglia and radial glia–a valuable tool for functional and lineage analysis. Glia *54*, 21–34. https://doi.org/10.1002/glia.20350.

Nam, S.C., Kim, Y., Dryanovski, D., Walker, A., Goings, G., Woolfrey, K., Kang, S.S., Chu, C., Chenn, A., Erdelyi, F., et al. (2007).

Dynamic features of postnatal subventricular zone cell motility: a two-photon time-lapse study. J. Comp. Neurol. *505*, 190–208. https://doi.org/10.1002/cne.21473.

Ninkovic, J., Mori, T., and Götz, M. (2007). Distinct modes of neuron addition in adult mouse neurogenesis. J. Neurosci. *27*, 10906–10911. https://doi.org/10.1523/jneurosci.2572-07.2007.

Rochefort, C., Gheusi, G., Vincent, J.-D., and Lledo, P.-M. (2002). Enriched odor exposure increases the number of newborn neurons in the adult olfactory bulb and improves odor memory. J. Neurosci. *22*, 2679–2689. https://doi.org/10.1523/jneurosci.22-07-02679.2002.

Schober, P., Boer, C., and Schwarte, L.A. (2018). Correlation coefficients: appropriate use and interpretation. Anesth. Analg. *126*, 1763–1768. https://doi.org/10.1213/ane.0000000000002864.

Snapyan, M., Lemasson, M., Brill, M.S., Blais, M., Massouh, M., Ninkovic, J., Gravel, C., Berthod, F., Götz, M., Barker, P.A., et al. (2009). Vasculature guides migrating neuronal precursors in the adult mammalian forebrain via brain-derived neurotrophic factor signaling. J. Neurosci. *29*, 4172–4188. https://doi.org/10.1523/JNEUROSCI.4956-08.2009.

Verleysen, M., and François, D. (2005). The Curse of Dimensionality in Data Mining and Time Series Prediction (Springer).

Waclaw, R.R., Ehrman, L.A., Pierani, A., and Campbell, K. (2010). Developmental origin of the neuronal subtypes that comprise the amygdalar fear circuit in the mouse. J. Neurosci. *30*, 6944–6953. https://doi.org/10.1523/jneurosci.5772-09.2010.

Yang, Z., and Klionsky, D.J. (2010). Mammalian autophagy: core molecular machinery and signaling regulation. Curr. Opin. Cell Biol. *22*, 124–131. https://doi.org/10.1016/j.ceb.2009.11.014.

Yuan, C., and Yang, H. (2019). Research on K-value selection method of K-means clustering algorithm. J *2*, 226–235. https://doi.org/10.3390/j2020016.

Zhang, J., Giesert, F., Kloos, K., Vogt Weisenhorn, D.M., Aigner, L., Wurst, W., and Couillard-Despres, S. (2010). A powerful transgenic tool for fate mapping and functional analysis of newly generated neurons. BMC Neurosci. *11*, 158. https://doi.org/10.1186/1471-2202-11-158.